

# Tribological Characteristics of Tungsten Carbide Reinforced Arc Sprayed Coatings using Different Carbide Grain Size Fractions

W. Tillmann<sup>a</sup>, L. Hagen<sup>a</sup>, P. Schröder<sup>a</sup>

<sup>a</sup>Institute of Materials Engineering, TU Dortmund University, Leonhard-Euler-Straße 2, 44227 Dortmund, Germany.

## Keywords:

Thermal sprayed coatings  
Carbide grain size fraction  
Arc spraying  
Tribological behavior  
WC-based cermet

## ABSTRACT

Tungsten carbide reinforced coatings play an important role in the field of surface engineering to protect stressed surfaces against wear. For thermally sprayed coatings, it is already shown that the tribological properties get mainly determined by the carbide grain size fraction. Within the scope of this study, the tribological characteristics of iron based WC-W<sub>2</sub>C reinforced arc sprayed coatings deposited using cored wires consisting of different carbide grain size fractions were examined. Microstructural characteristics of the produced coatings were scrutinized using electron microscopy and x-ray diffraction analyses. Ball-on-disk test as well as Taber Abraser and dry sand rubber wheel test were employed to analyze both the dry sliding and the abrasive wear behavior. It was shown that a reduced carbide grain size fraction as filling leads to an enhanced wear resistance against sliding. In terms of the Taber Abraser test, it is also demonstrated that a fine carbide grain size fraction results in an improved wear resistant against abrasion. As opposed to that, a poorer wear resistance was found within the dry sand rubber wheel tests. The findings show that the operating mechanisms for both abrasion tests affect the stressed surface in a different way, leading either to microcutting or microploughing.

## Corresponding author:

Leif Hagen  
TU Dortmund University,  
Leonhard-Euler-Straße 2,  
44227 Dortmund,  
Germany.  
E-mail: leif.hagen@tu-dortmund.de

© 2017 Published by Faculty of Engineering

## 1. INTRODUCTION

The life span of industrial components is limited by its wear and corrosion resistance. Due to the increasing demand on productivity, quality, and efficiency, the performance related stress on functional surfaces such as tool surfaces and machine parts is increased at the same time. Thermal spraying becomes one of the most versatile and economical surface technologies to

apply hard coatings, which provide superior tribological characteristics.

Tungsten carbides reinforced coatings are widely established in the field of surface engineering to protect functional surfaces against wear. For various thermal spray techniques, numerous studies emphasized the enhanced wear resistance of WC reinforced coatings against sliding wear [1], abrasive wear

[2] as well as erosion [3] and erosion–corrosion [4]. For high velocity oxy fuel [5, 6], plasma [7,8] and suspension flame [9] sprayed coatings, several authors investigated the tribological characteristics of stressed surfaces by employing different tungsten carbide grain-sized feedstocks. It was found that a decreased carbide grain size possesses a higher resistance against abrasion, sliding, or erosive wear.

In comparison to other thermal spray techniques, twin wire arc spraying (TWAS) process is a time saving [10] and energy efficient [11] process mainly used in surface refurbishments and maintenance applications [12]. Nevertheless, TWAS provides the ability to deposit hard coatings, such as tungsten carbide reinforced composites, accompanied by cost saving measures due to the use of compressed air and cored wires with hard particle filling, which serves as atomization gas, and feedstock, respectively. Consequently, tungsten carbide reinforced arc sprayed coatings appear to be an appropriate candidate to protect stressed surfaces against wear. In terms of arc sprayed coatings, only few studies have discussed the use of tungsten carbide reinforced feedstocks such as iron-based (FeCrSiMn-WC/W<sub>2</sub>C, Fe<sub>3</sub>Al-WC, Fe-FeB-WC) [13-16] and nickel-based alloys ((NiCrBSi, NiBSi)-WC/W<sub>2</sub>C, Ni-(WC-Co)) [12, 17, 18]. With respect to the feedstock, Ni-based and Co-based materials exhibit some health and safety issues. Bolelli et al. [19] already discussed their toxicity and health hazard in thermal spray processes, referring to a hazard statement according to European Commission regulation (EC) No. 790/2009 [20] and a “Report on Carcinogens” [21]. As opposed to that, Fe-based alloys have turned out to be less hazardous when compared to Ni- and Co-based alloys. Thus, tungsten carbide reinforced Fe-based MMCs constitute an environmentally friendly alternative for thermal spray applications. In terms of WC and WC-W<sub>2</sub>C reinforced Fe-based arc sprayed coatings, different studies focused on the tribological behavior [13, 15, 16]. According to these studies, the samples were either produced with agglomerated sintered WC-Co powders or with the use of coarse grain-sized eutectic carbides. The utilization of different grain-sized tungsten carbides was not taken into account.

With respect to the tribo-mechanical properties of arc sprayed coatings, the microstructural characteristics, such as the microstructure formation, the amount of hard phases and phase composition, play a significant role. To the best of our knowledge the phase evolution of arc sprayed Fe-based WC-W<sub>2</sub>C reinforced coating systems has not been examined. Only a few studies investigated the microstructure formation and phase transformation of arc sprayed Ni-based WC-W<sub>2</sub>C reinforced coating systems [12, 17]. According to these studies, eutectic tungsten carbides decarburize during spraying and a large amount of W dissolves into the Ni-rich matrix. It was mentioned that these metallurgical interactions affect the mechanical properties of the produced coating systems. Among others such as the chemical composition of the metal matrix, the degree of dissolution of tungsten carbides depends on the type, shape and size. For instance, irregular shaped particles are more prone to dissolve due to the tendency to heat up to higher temperatures through the exposure of a heat source [22]. Small sized particles tend to dissolve faster than coarser. Moreover, as reported by other researchers [23, 24] eutectic tungsten carbides are more prone to react with the liquid melt, than more thermally stable carbides such as mono crystalline carbides consisting of hexagonal WC.

In this study, the tribological characteristics of Fe-based WC-W<sub>2</sub>C reinforced arc sprayed coatings deposited using cored wires consisting of different carbide grain size fractions were investigated. In order to examine the sliding and abrasive wear behavior, ball-on-disk test as well as Taber Abraser, and dry sand rubber wheel test were conducted. Those tribological tests selected appear to stress the coating surfaces in different ways without the need of time-consuming and expensive field tests. Accordingly, wear effects and wear mechanisms of stressed surfaces were assessed for both samples types (manufactured with the use of a conventional and fine carbide grain size fraction). Moreover, the microstructure formation of the produced coating systems was scrutinized by using electron microscopy and energy disperse x-ray spectroscopy. The phase evolution after spraying across the samples was analyzed via x-ray diffraction.

## 2. EXPERIMENTEL

### 2.1 SUBSTRATE AND FEEDSTOCK MATERIAL

Round (with  $d = 40$  mm for the ball-on-disk test, and  $d = 105$  mm for the Taber Abraser test) and rectangle (20 mm x 65 mm x 10 mm for the dry sand rubber wheel test) C45 steel specimens were used as substrate material. Prior coating deposition, the samples were grit-blasted (corundum EKF 14) and cleaned after in an ultrasonic ethanol bath for 15 minutes.

An iron-based (2 wt.% C, <1 wt.% Mn, 1.4 wt.% Si, bal. wt.% Fe) cored wire with 50 wt.% of cast tungsten carbides CTC (eutectic mixture of WC and  $W_2C$ ) as filling serves as feedstock (type Durmat AS-850, Fa. Durum Verschleisschutz, Germany) for the coating deposition. Two different wire types were used in this study. Both FeCMnSi based cored wires feature a diameter of 1.6 mm (band width of the velum: 10 mm, thickness of the velum: 220  $\mu\text{m}$ ). Regarding the wire configuration used in this study, two different carbide grain size fractions (conventional and fine) serve as fillings (Fig. 1).

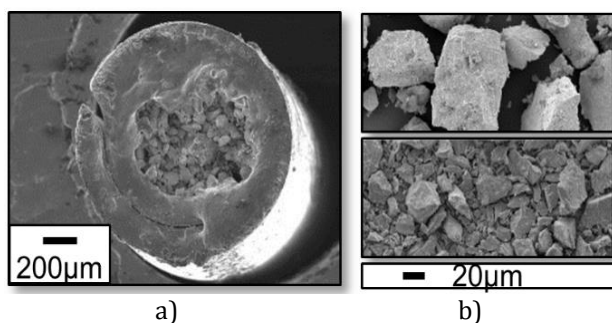


**Fig. 1.** (a) wire configuration used in this study; (b) different carbide grain size fractions which serve as filling (top: coarse carbide grain-sized filling; down: fine carbide grain-sized filling).

As observed by laser light scattering using the particle analyzer S3500 (Fa. Microtrac, Pennsylvania), the conventional carbide grain-sized filling features a bimodal particle size distribution with a fine proportion in the small micrograin range. Regarding the volumetric size distribution, the 50<sup>th</sup> percentile of the sampling is  $d_{P50} = 113.2 \mu\text{m}$  ( $d_{P10} = 72.8 \mu\text{m}$ ,  $d_{P90} = 158.4 \mu\text{m}$ ). As opposed to that, the 50<sup>th</sup> percentile of the sampling of the fine grain-sized filling is  $d_{P50} = 38.7 \mu\text{m}$  ( $d_{P10} = 22.3 \mu\text{m}$ ,  $d_{P90} = 66.0 \mu\text{m}$ ).

### 2.3 SPRAYING PARAMETERS

The Smart Arc 350 PPG arc spraying system (Fa. Oerlikon Metco, Switzerland) was utilized for the coating deposition using two overruns. All parameters were kept constant for both sample types (1,6 as referred to the conventional carbide grain size fraction; 1,6 UF as referred to the fine carbide grain size fraction). According to the spray parameters, the voltage and current were set to 30 V and 220 A, respectively. For the atomization gas, compressed air with a gas pressure of 0.6 MPa was used. In terms of the handling parameters of the spray torch, a spray distance of 110 mm, gun velocity of 200 mm/s, and track pitch of 5 mm were utilized.

### 2.4 ANALYTIC METHODS

In order to analyse the coated samples by means of electron microscopy, the samples were separated and prepared using the following steps: plane grinding, fine grinding, and polishing. For the polishing, polishing cloths with a diamond suspension of 9  $\mu\text{m}$ , 6  $\mu\text{m}$ , 3  $\mu\text{m}$ , and 1  $\mu\text{m}$  grain-sized particles were employed. Cross-section images were taken by a field emission scanning electron microscope (FE-SEM) type JSM-71001F (Fa. Jeol, Germany). The distribution of elements was analyzed by using energy dispersive x-ray spectroscopy (EDX) with the integrated software INCA (Fa. Oxford Instruments, United Kingdom).

The phase evolution in the produced sample types was analysed by means of x-ray diffraction (XRD) using synchrotron radiation. Thus, the experiments were conducted at beamline BL9 of the synchrotron light source DELTA [25] (Dortmund, Germany). The incident photon energy was 27 keV (wavelength  $\lambda = 0.4592 \text{ \AA}$ ). The angle of incidence was set to 5 degrees and a beam-size of  $0.2 \times 1.0 \text{ mm}^2$  ( $v \times h$ ) was utilized. The scattered intensity was measured using a MAR345 image plate detector. The diffraction patterns were obtained from the MAR images by using a FIT2D program package [26]. Subsequently, the 2 theta scale of the diffraction patterns was converted to a wavelength of  $\lambda = 1.5406 \text{ \AA}$ , which corresponds to Cu-K $\alpha$  radiation. Prior tribological examination of the different sample types, the surface of all coated specimens was machined and polished, using a silicon carbide grinding disk (4000 fine grit) and

polishing cloths with a diamond suspension (3 and  $1/4 \mu\text{m}$ ). A ball-on-disk (BOD) tribometer (Fa. CSM, Switzerland) was used to analyse the friction and wear behavior against sliding. The experiments were conducted with a load of 10 N using an alumina ball (diameter of 6 mm) as a counterbody. A constant track radius of 12 mm and a velocity of 40 cm/s were selected. The tests were carried out by utilizing 30,000 revolutions. Subsequently, the volume loss of the stressed surfaces caused by dry sliding experiments was analyzed by using 3D-profilometry (Fa. Alicona, Austria). Four different spots on three samples for each sample type were surveyed. Based on the average volume loss across the wear track, the normal force applied in the test as well as the sliding distance, the wear coefficient was determined for both the coated specimen ( $k_{BOD}$ ) and counterbody ( $k_{counterbody}$ ), respectively.

In view of the abrasion tests, two standardized tests with different characteristics and grain size fractions of abrasive particles were utilized. On the one hand, the dry sand rubber wheel (DSRW) test was employed considering the relevant ASTM standard [27]. A rubberized tire (shore hardness A58-62) with an external diameter of 227.6 mm, a breadth of 12.7 mm, and a thickness of 10 mm was utilized. The rotating speed was  $195 \text{ min}^{-1}$ . Rounded silica sand serves as abrasive particle (Fig. 2a).

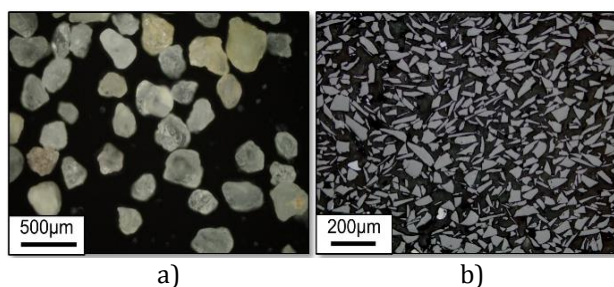


**Fig. 2.** Optical micrographs showing the abrasive particles used for the a) DSRW Test and b) Taber Abraser test.

The particle aspect ratio (ARp) (ratio of the maximum Feret diameter to the minimum Feret diameter) was determined by image analysis (software: Olympus stream motion, Fa. Olympus, Germany) using light micrographs (optical microscope: type Olympus BX51M and Olympus DP25, Fa. Olympus, Germany) taken twenty different spots of an embedded sampling into account. The average value of ARp for the silica

sand particles was 1.47. Regarding the particle size distribution, the 50<sup>th</sup> percentile of the sampling is  $d_{P50} = 252.70 \mu\text{m}$  ( $d_{P10} = 86.96 \mu\text{m}$ ,  $d_{P90} = 333.42 \mu\text{m}$ ). The Vickers hardness of the silica particles was measured as  $1392 \pm 46 \text{ HV0.3}$ . The feed rate for the abrasives was kept on a constant level of 340 g/min. The applied load with which the specimens are pressed to the rubberized tire was 130 N. Five specimens of each sample type were employed. The mass loss of each sample was measured before and after testing using 1004 revolutions, which corresponds to a distance of approx. 718 m.

On the other hand, the Taber Abraser test (type 505 Dual Abrasion Tester, Fa. Taber Industries, New York) was conducted. The Calibrade H10 (vitrified bonded) was installed as abrading wheel. Figure 2b illustrates the morphology of the abrasive particles with their surrounded vitrified bond. The average value of ARp for the abrasive particles was 2.62, whereas the maximum and minimum values varied significantly. As obtained from image analysis, the 50<sup>th</sup> percentile of the particle size distribution of the sampling is  $d_{P50} = 16.24 \mu\text{m}$  ( $d_{P10} = 2.83 \mu\text{m}$ ,  $d_{P90} = 39.47 \mu\text{m}$ ). The Vickers hardness of the abrasive particles was measured as  $2585 \pm 268 \text{ HV0.3}$ . With respect to the test parameter settings, a load of 9.81 N, and rotating speed of 60 rpm was applied. The tests were carried out on a constant track (track diameter = 74 mm) with a total amount of 40,000 cycles. Regarding the examination procedure, the abrasive wear test was interrupted after each 1,000 cycles. Following an interruption, the samples were taken out, cleaned with compressed air and weighted. In order to provide same stress state conditions, the abrading wheels were dressed (reconstitute sharpness) and also cleaned (remove debris) with compressed air. The gravimetric abrasive wear coefficient  $k_{gTA}$  for both sample types were calculated considering the specific weight loss of the worn surface, the applied load, and the rolling wear distance. For all three tribological tests, a lower calculated wear coefficient  $k_{BOD}$  (related to the dry sliding experiments),  $k_{DSRW}$  (related to the DSRW test), and  $k_{gTA}$  (related to the Taber Abraser test) is accompanied by a higher resistance of the coating against wear.

In addition, the wear effects and wear mechanisms, which occurred within dry sliding

and abrasive wear tests, were scrutinized by electron microscopy. Moreover, the coating surface area was characterized by means of nanoindentation determining the Young's modulus and hardness. With respect to the mechanical properties, 49 indents were conducted on the top surface under penetration-control mode (maximum depth of 2,000 nm). Load and displacement sensing indentation, which is described in a work by Oliver and Pharr [28], was carried out using the nanoindenter type G200 (Fa. Agilent Technology, USA) with a Berkovich indenter. As far as indentation size effects can be an issue and in order to get more reliable results, Brinell hardness was determined according to DIN EN ISO 6506-1 with a universal hardness tester DIA-TESTOR 7521 (Fa. Wolpert, Germany) on the top surface. The measurements were conducted using a carbide ball with a diameter of 1 mm at a load of 98.07 N. The diameter of the remaining indentation was measured with an optical microscope type Axiophot (Fa. Zeiss, Germany) with integrated image analysis software Axiovision Aut-mess. The Brinell hardness of each sample was calculated taken three indents into account.

### 3. RESULTS

#### 3.1 MICROSTRUCTURAL CHARACTERISTICS

Figure 3 shows SEM images of cross-sections of different sample types produced with the use of the conventional carbide grain-sized filling (sample 1,6), and fine carbide grain-sized filling (sample 1,6 UF). For both samples, the variation of the brightness suggests inhomogeneity in the chemical composition.

Quantitative EDX analyses reveal that the layers are formed from lamellar microstructure of Fe-rich and W-rich phases. Accordingly, W-rich hard particles (bright phases) scatter throughout the coatings and are surrounded by the iron-based matrix (dark grey phases). It is obvious that the distribution of the hard particles is very heterogeneous. Occasionally, pores and some intergranular cracks occur across the coatings. These cracks pass along grain boundaries between different lamellar splats. In a few cases, not fully fused W-rich hard phases are observed. These particles consist of a polygonal shape.

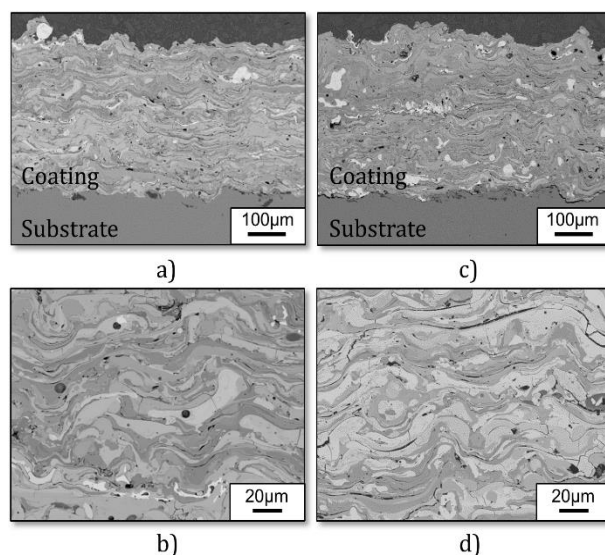


**Fig. 3.** SEM images showing the cross-sections of a, b) sample 1,6 and c, d) sample 1,6 UF.

The distribution of elements across the coating was determined by means of EDX analyses. To compare the different samples qualitatively, light elements (in this case C and O) were omitted. Results taken from the EDX analyses at different areas across the deposits were considered to calculate the mean average of W. For the sample 1,6, the mean average was  $41.9 \pm 0.4$  wt.% of W, whereas the sample 1,6 UF consists of  $38.4 \pm 0.8$  wt.% of W. Based on these results, it can be stated that the sample 1,6 obtain a higher content of W-rich hard phases. However, when compared to the starting cored wire materials some carbide loss was ascertained as a reduced amount of W was observed across deposits.

In terms of the phase composition, XRD analysis reveals the evidence of phase transformation processes such as dissolution of eutectic carbides and the formation of ternary phases. XRD analysis confirms that the velum is mainly composed of Fe, while the filling consists of the eutectic phases WC and  $W_2C$  (data not shown). Figure 4 shows the XRD patterns of the samples 1,6 and 1,6 UF. It is observed that both samples 1,6 and 1,6 UF are mainly composed of eutectic carbides (WC and  $W_2C$ ), eta carbides ( $Fe_2W_2C$ ,  $Fe_3W_3C$ ,  $Fe_6W_6C$ ,  $FeW_3C$ ), elementary tungsten, and some carbide phases ( $Fe_2C$ ,  $Fe_3C$ ,  $Fe_4C$ ,  $C_{0.08}Fe_{1.92}$ ,  $CFe_{15.1}$ ). However, the results reveal that the presence of eta carbides such as  $FeW_3C$  and  $Fe_6W_6C$  is more pronounced in sample 1,6 UF with the use of the fine carbide grain size fraction as filling.

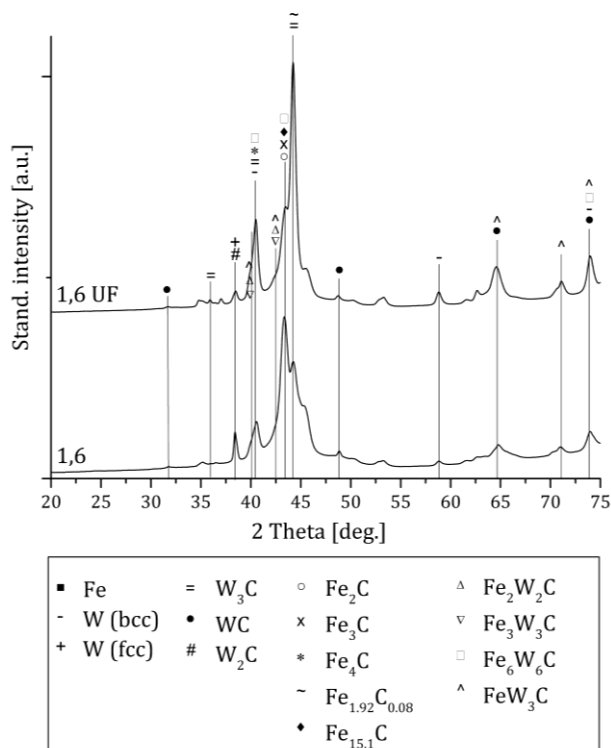


**Fig. 4.** XRD patterns of samples 1,6 and 1,6 UF. The 2 Theta axis is scaled to a photon energy of 8 keV.

The hardness and Young’s modulus as well as the ratio between them were analyzed due to their relation to the mechanical properties of the coating as shown in [29,30]. In Fig. 5, it is visible that the carbide grain size fraction used for coating deposition affects the mechanical properties.

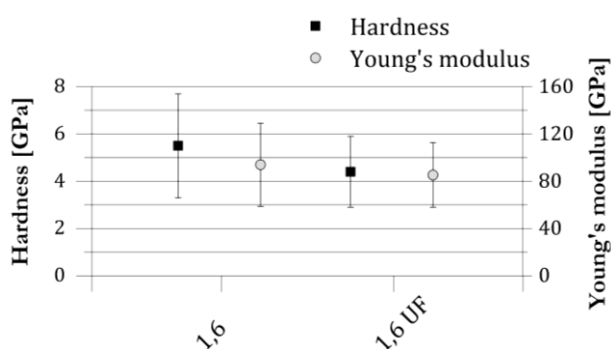


**Fig. 5.** Hardness and Young’s modulus of different samples.

As shown by nanoindentation, a finer carbide grain size fraction causes a decrease in hardness and Young’s modulus. Hence, the value for hardness decreases from  $5.5 \pm 2.2$  GPa (sample 1,6) to  $4.4 \pm 1.5$  GPa (sample 1,6 UF). Taken the  $H^3/E^2$ -ratio into account, the coating deposited with a conventional carbide grain size fraction

features a slightly increased  $H^3/E^2$ -ratio as it rises from 0.011 (sample 1,6 UF) to 0.019 (sample 1,6). According to the macrohardness, the samples 1,6 and 1,6 UF possess a Brinell hardness of  $242 \pm 17$  HBW 1/10, and  $220 \pm 23$  HBW 1/10 respectively.

### 3.1 DRY SLIDING EXPERIMENTS

In dry sliding operations such as the BOD tests, the wear coefficient  $k_{BOD}$  was determined by the volumetric wear loss of the stressed surfaces of both sample types (1,6 and 1,6 UF). Taken from the measurements by means of 3D profilometry, it is observed that a fine carbide grain size fraction leads to a significant decrease in  $k_{BOD}$ , which in turn reveals an enhanced wear resistance against sliding (Fig. 6a).

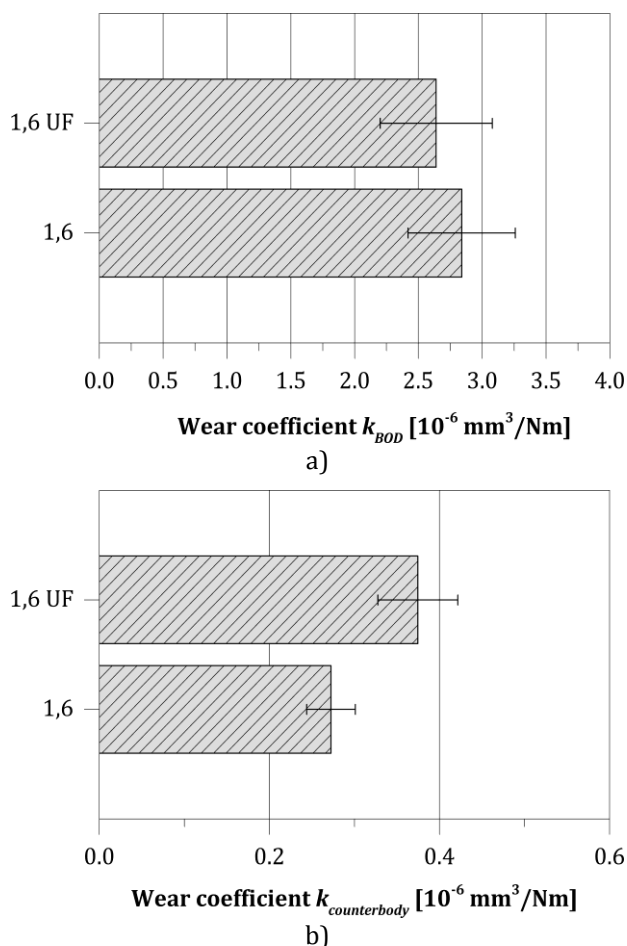


**Fig. 6.** a) Wear coefficient  $k_{BOD}$  of samples in dry sliding experiments against alumina; b) wear coefficient  $k_{Counterbody}$  of the alumina counterbody sliding against sample 1,6 and 1,6 UF.

Accordingly, sample 1,6 UF exhibits a value for  $k_{BOD}$  of  $2.64 \times 10^{-6} \text{ mm}^3/\text{Nm}$ , whereas sample 1,6 possesses a  $k_{BOD}$  of  $2.84 \times 10^{-6} \text{ mm}^3/\text{Nm}$ .

For analyzing the whole tribological system, the volume loss of the counterbody in form of an alumina ball is determined. Figure 6b shows the wear coefficient  $k_{Counterbody}$  of the alumina ball. In view of the counterbody, the results obtained from the 3D-profilometry show a different extent of wear. Thus, the counterbody sliding against sample 1,6 UF exhibits a  $k_{Counterbody}$  of  $0.37 \times 10^{-6} \text{ mm}^3/\text{Nm}$ . As opposed to that, the counterbody sliding against sample 1,6 possesses a  $k_{Counterbody}$  of  $0.27 \times 10^{-6} \text{ mm}^3/\text{Nm}$ .

The findings encourage the assumption that the sample 1,6 UF (produced with a finer carbide grain size fraction) boasts an enhanced wear resistance against sliding, which in turn leads to an increased attrition of the alumina counterbody.

With respect to the friction behavior, the results obtained in dry sliding experiments show a reduced coefficient of friction (COF) for sample 1,6 UF, when compared to sample 1,6 (Fig. 7).

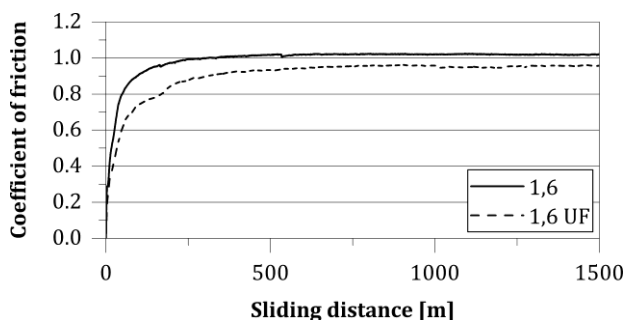


Fig. 7. Coefficient of friction of different samples sliding against alumina.

In consideration of the run-in behavior, the sample 1,6 UF exhibits a COF of 0.95 (mean value of 0.91). In comparison, sample 1,6 possesses a COF of 1.02 (mean value of 0.99). Thus, the results obtained from the dry sliding tests reveal an improved friction behavior for the sample deposited with the use of a fine carbide grain size fraction as shown by a reduced COF against alumina.

### 3.2. ABRASIVE WEAR EXPERIMENTS

For analyzing the abrasive wear behavior of the coating systems, two commonly used abrasive wear tests (Taber Abraser test, DSRW test) were applied. Concerning the Taber Abraser test, it is shown that a reduction in carbide grain size fraction leads to a significant decrease of the wear coefficient  $k_{TA}$  (Fig. 8).

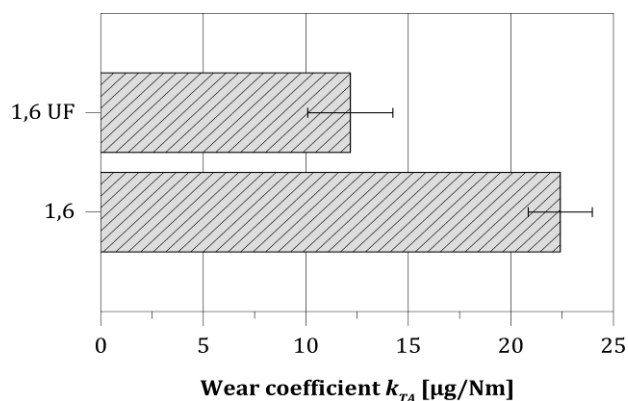


Fig. 8. Wear coefficient  $k_{TA}$  of different samples obtained by the Taber Abraser test.

Thus, the sample 1,6 UF obtains a  $k_{TA}$  of  $12.17 \pm 2.08 \text{ µg/Nm}$ . By comparison, the gravimetric measurement of the material loss of the stressed surface of sample 1,6 reveals a  $k_{TA}$  of  $22.41 \pm 1.56 \text{ µg/Nm}$ .

Regarding the DSRW test, a different tendency could be observed (Fig. 9). Accordingly, the sample 1,6 UF exhibits a higher mass loss, when compared to sample 1,6, resulting in an increased wear coefficient  $k_{DSRW}$ . Thus, sample 1,6 UF features a  $k_{DSRW}$  of  $2.61 \pm 0.11 \text{ µg/Nm}$ , whereas the sample 1,6 reveals a  $k_{DSRW}$  of  $2.26 \pm 0.08 \text{ µg/Nm}$ .

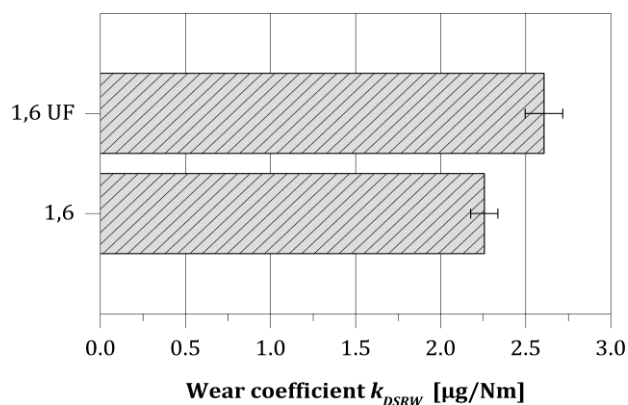


Fig. 9. Wear coefficient  $k_{DSRW}$  of different samples obtained by the dry rubber wheel test.

With respect to  $k_{DSRW}$  of both sample types, the deposit produced with a fine carbide grain size fraction possesses a poorer resistance against abrasive wear when compared to the deposit manufactured with a conventional carbide grain size fraction. Nevertheless, by comparison of both wear coefficients,  $k_{TA}$  and  $k_{DSRW}$ , the findings show that the samples 1,6 and 1,6 UF experience a more severe wear in the Taber Abraser test by contrast with the DSRW test.

## 4. DISCUSSION

### 4.1 MICROSTRUCTURE

XRD analyses on stressed surfaces reveal the formation of eta carbides as shown in Fig. 4. When compared to the deposit sprayed with the conventional grain-sized filling, the sample produced with the use of the fine carbide grain-sized filling is more prone to consist of ternary carbides, which can be assigned to  $\text{Fe}_6\text{W}_6\text{C}$  and  $\text{FeW}_3\text{C}$ .

With respect to the eutectic carbides (eutectic mixture of WC- $\text{W}_2\text{C}$ ), which serve as filling,  $\text{W}_2\text{C}$  makes the largest share with 73-80 wt.%. Stoichiometric WC has a carbon content of 6.13 wt.%, whereas  $\text{W}_2\text{C}$  has a low carbon content of 3.61 wt.% [31]. Eta carbides (e.g.  $\text{M}_3\text{W}_3\text{C}$ ,  $\text{M}_6\text{W}_6\text{C}$  etc.) are mainly formed according to Suetin et al. [32] with heterogeneous microstructures, especially in the interface of WC and the transitional metal. The stoichiometries as well as the matrix material influence the phase stability [33,34].

The microstructure formation of arc sprayed Fe-based MMC composites using eutectic tungsten carbides has not been extensively examined. In contrast, a few studies investigated the microstructure formation and phase transformation of arc sprayed Ni-based WC- $\text{W}_2\text{C}$  reinforced coating systems [12,17]. According to these studies, tungsten carbide decarburized during spraying and a large amount of W dissolved into the Ni-rich matrix. Besides W dissolving into Ni-matrix, Ni also dissolved into WC- $\text{W}_2\text{C}$  and gathered around WC- $\text{W}_2\text{C}$  grains to form fine WC- $\text{W}_2\text{C}$ -Ni composites. It was stated that these metallurgical interactions are attributed to the electrode phenomena during atomization, when the WC- $\text{W}_2\text{C}$  grains are wetted by the molten metal.

In terms of WC-Fe composites, research activities linked to the development of WC-reinforced Fe-based alloys by means of laser melt interjection [35] showed that small WC and  $\text{W}_2\text{C}$  isles formed around the WC particles at low processing temperatures. Higher processing temperatures, however, lead to the formation of further transition zones, with strongly varying elementary W and C [36]. According to a study by Zhou et al. [37], the solubility of W in Fe is

influenced by the WC particle size. Thus, the solubility of W increases to the surrounding Fe-matrix with a decreasing WC particle size. At this point, it is not yet clear in how far these process conditions can be adapted to arc spraying processes.

However, the degree of dissolution of the tungsten carbide also depends on the type, shape and size of tungsten carbide. For instance, irregular shaped particles are more prone to dissolve due to the tendency to heat up to higher temperatures through the exposure of a heat source [22]. Small sized particles tend to dissolve faster than coarser. Moreover, as reported by other researchers [23,24] eutectic tungsten carbides are more susceptible to react with the liquid melt, when compared to more thermally stable carbides such as mono crystalline carbides consisting of hexagonal WC.

With respect to the findings gained by Brinell hardness measurement and nanoindentation (Fig. 5), it can be stated that sample 1,6 UF provides a reduced hardness when compared to sample 1,6. As far as XRD analysis reveals the partially dissolution of eutectic tungsten carbides and the formation of eta carbides, those metallurgical interactions might affect the mechanical response of the stressed surface. Mechanical properties such as hardness and Young's modulus of different phases of the Fe-W-C-system can be found in literature [32-34, 38-44]. Relevant carbides and others are listed in the following Table 2.

**Table 2.** Hardness and Young's modulus of relevant carbides and other phases.

	Young's modulus [GPa]	Hardness [GPa]
<b>Eta carbides</b>		
$\text{Fe}_2\text{W}_2\text{C}$ [34]	274.5	7.63
$\text{Fe}_3\text{W}_3\text{C}$ [32-34]	446.1-469.7	15.6-16.8
$\text{Fe}_6\text{W}_6\text{C}$ [32, 34]	446.6	14.73-15.6
$\text{Fe}_{21}\text{W}_2\text{C}_6$ [34]	437.6	14.99
<b>Tungsten Carbides</b>		
h-WC [34, 39, 42]	690.9-697	16-22
WC [40, 44]	710	23.5
h- $\text{W}_2\text{C}$ [42]	479.6	
o- $\text{W}_2\text{C}$ [42]	437.2	
t- $\text{W}_2\text{C}$ [42]	427.3	
$\text{W}_2\text{C}$ [40, 43, 44]	420-444	29.4
<b>Others</b>		
Fe [38, 41]	141	
W [41, 43]	400-410	
$\text{Fe}_3\text{C}$ [33, 34, 40]	306-311.04	

According to these findings obtained in numerous studies, eta carbides such as  $M_4C$ ,  $M_6C$ ,  $M_{12}C$  and  $M_{23}C_6$  phases provide a reduced hardness when compared to WC and  $W_2C$ .

### 4.3 SLIDING WEAR BEHAVIOR

It is found that the use of a fine carbide grain size fraction as filling leads to an enhanced sliding wear behavior as shown by a reduced  $k_{BOD}$  (Fig. 6a). This phenomenon was also demonstrated in a study by van Acker et al. [45]. Thus, the authors examined the effect of the tungsten carbide particle size and distribution on the wear resistance of laser clad WC-Ni coatings. For alumina as a counterbody in dry sliding experiments, it was shown that an increased concentration of carbides as well as a decrease in their size are both favorable for the wear resistance.

Figure 10 shows the worn surfaces after dry sliding experiments. Breakouts are clearly visible and their extent differs in terms of their dimensions when comparing sample 1,6 and 1,6 UF.

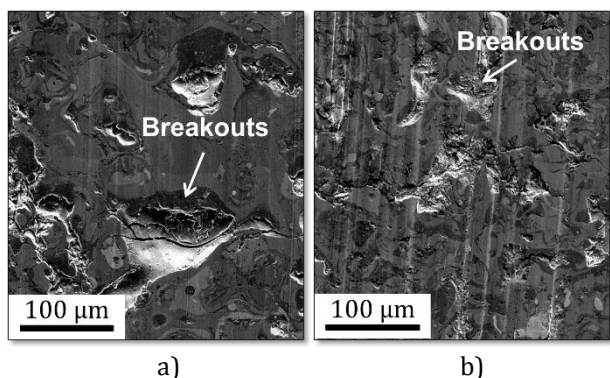


**Fig. 10.** Wear tracks after ball-on-disk test: a) sample 1,6, and b) sample 1,6 UF.

Those wear effects result from fatigue and extensive load caused by Hertzian stress and are also promoted by cyclical movement of the alumina ball over the coating surface. If the carbides (eutectic carbides or eta carbides) are of larger size, the whole Hertzian stress in the contact zone has to be withstood by only one or a few carbides. At the same time, the inherent process characteristics of arc spraying lead to the formation of a brittle metallic binder phase surrounding those carbides. Due to the embrittlement, those embedded carbides consequently suffer from the mechanical cycling

loads, which results in crack initiation. If the load is particularly severe, the cracks further propagate and lead to a carbide breakage. The fragmentation of those carbides can easily promote the development of breakouts, even where the carbides are partial metallurgically bonded.

Moreover, both samples (1,6 and 1,6 UF) show mechanical abrasion such as grooves. It can be stated that third-body wear originated by small fragments, which are detached from the stressed surface (e.g. fractured carbides) or the counterbody. The extent of grooves was more pronounced for sample 1,6 UF as an increased amount of small abrasive particles pass through the contact zone.

In terms of Ni-based WC- $W_2C$  reinforced arc sprayed coatings, similar wear effects and mechanisms have been observed. Accordingly, Sheppard and Koiprasert [12] found that craters on the stressed surface are the result of WC- $W_2C$  detachments during sliding wear tests. It is reported that stress induced by the sliding operation promotes intergranular cracks to propagate, and thus, WC- $W_2C$  to be pulled-out. It is also mentioned that the amount and extent of craters depend on the intersplat bonding.

Consequently, arc sprayed deposits produced with the use of a fine carbide grain size fraction as filling lead to an enhanced wear resistance against sliding, since the load within the test is distributed to a larger amount of carbides. The findings also encourage the assumption that a carbide breakage due to the pitting formation is more likely for larger carbides, thus, the probability of extrusion is higher. Same interrelationship was also found in [2, 3] for HVOF sprayed WC reinforced coatings.

### 4.4 FRICTION BEHAVIOR

The sample 1,6 UF, produced with the fine carbide grain size fraction, features an enhanced friction behavior as it can be seen by a reduced COF (Fig. 7). Metallographic investigations reveal that the sample 1,6 UF consists of a finer lamellar microstructure. Accordingly, the microstructure is characterized by slightly shortened narrow flakes and lamellas. However, W-rich hard phases are heterogeneously scattered across the coating. Nevertheless, those

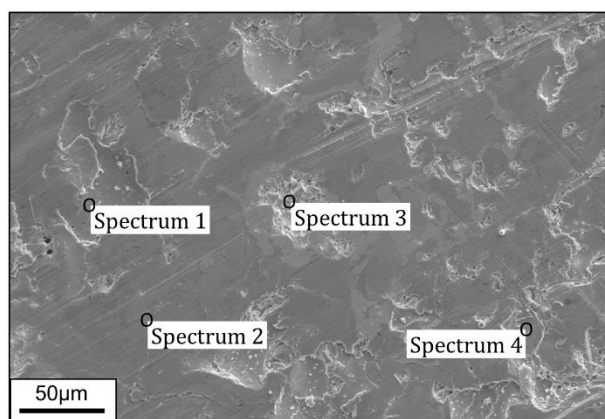
fine lamellas and fine-structured W-rich hard phases possess an enhanced support for the alumina counterbody at the contact area, which in turn leads to a reduced friction. Similar findings have already been observed for HVOF sprayed WC reinforced cermet coatings using different WC grain-sized feedstocks [46].

#### 4.5 ABRASIVE WEAR BEHAVIOR

The two abrasion tests selected appear to stress the surface of the coatings in a different way indicating that different wear mechanisms occur. For both sample types (sample 1,6 and 1,6 UF), the Taber Abraser test produces a grid of intersecting lines (Fig. 11) due to the circular movement, whereas the DSRW test generates a pattern of parallel scratch lines (Fig. 12).

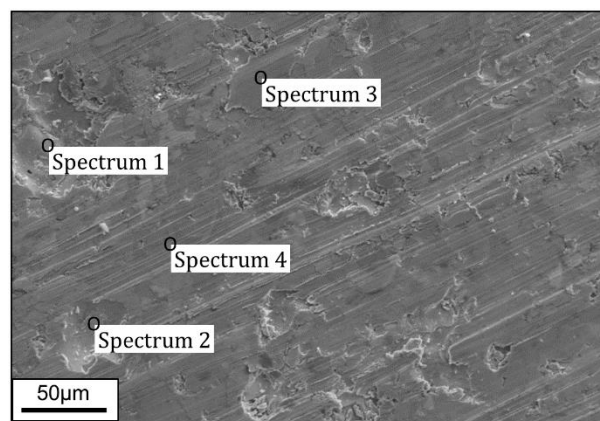
All sample types suffer abrasion concerned by a combination of microcutting and micro-ploughing. As observed in this study, the Taber Abraser test causes for both samples an apparently more severe abrasion when compared to the DSRW test (Fig. 11 and Fig. 12).

In terms of the Taber Abraser test, the operating mechanism (particle impact) changed from microcutting to delamination wear. Breakouts were observed for both stressed surfaces across the wear track by electron microscopy (Fig. 11a and b).



	Element concentration in wt.%			
	C	Fe	O	W
<b>Spectrum 1</b>	0.35	80.70	5.07	13.88
<b>Spectrum 2</b>	0.14	50.91	4.02	44.93
<b>Spectrum 3</b>	0.97	10.46	5.38	83.19
<b>Spectrum 4</b>	0.81	51.17	7.46	40.56

a)



	Element concentration in wt.%			
	C	Fe	O	W
<b>Spectrum 1</b>	0.69	34.72	3.28	61.32
<b>Spectrum 2</b>	0.71	42.83	4.71	51.75
<b>Spectrum 3</b>	0.77	60.41	2.99	35.82
<b>Spectrum 4</b>	0.23	56.48	3.13	40.16

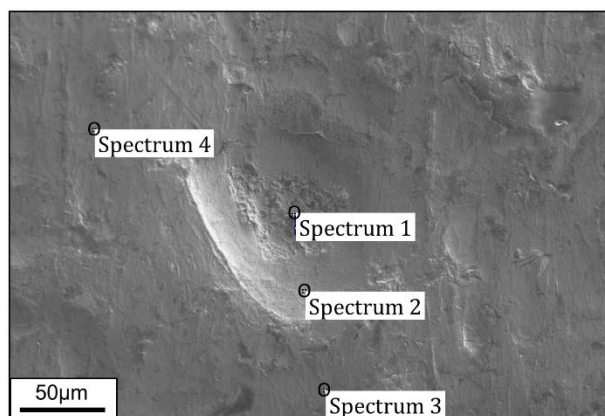
b)

**Fig. 11.** SEM images and EDX spot analyses showing the worn surface and its element concentration after Taber Abraser test: a) sample 1,6, and b) sample 1,6 UF.

Debris mainly consists of W-rich hard phases. A fractured surface with a honeycomb structure indicates the fragmentation of W-rich hard phases. Results taken by EDX analysis (Fig. 11a, spectrum 3) reveal the presence of an increased amount of W, which encourages the assumption that subsurface fatigue of W-rich hard phases occurs. Subsequently, micro fractures and cracks emerged, leading to the fragmentation and disruption of carbides. As a consequence, fragmented W-rich hard phases were torn out. For sample 1,6, those breakouts and pits were larger, leading to an increased gravimetric material loss as shown by an increased  $k_{TA}$  (Fig. 8). Thus, a fine carbide grain size fraction as filling leads to an enhanced wear resistance of sample 1,6 UF as depicted by a decreased  $k_{TA}$ .

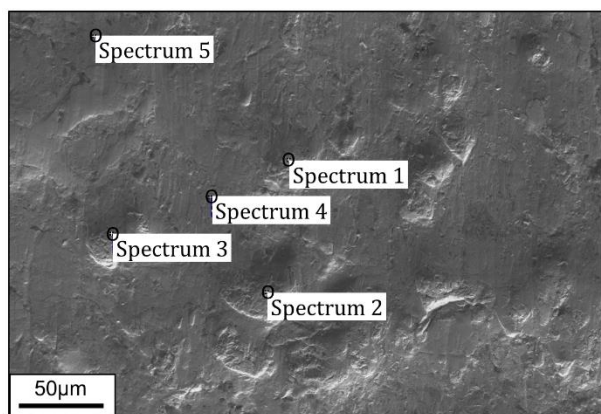
As opposed to that, a reduced wear resistance was revealed in DSRW test for sample 1,6 UF when compared to sample 1,6. Thus, sample 1,6 exhibits a lower  $k_{DSRW}$  as demonstrated in Fig. 9. SEM images of the worn surface of sample 1,6 and 1,6 UF show that the stressed surface is characterized by some cavities and pits which differ in their size and extent for sample 1,6 and 1,6 UF (Fig. 12). Accordingly, larger pits are observed for sample 1,6 (Fig. 12a), whereas

heterogeneously distributed smaller pits occurred for sample 1,6 UF (Fig. 12b).



	Element concentration in wt.%			
	C	Fe	O	W
<b>Spectrum 1</b>	8.11	0.60	11.85	79.44
<b>Spectrum 2</b>	5.83	16.05	5.67	72.45
<b>Spectrum 3</b>		31.37	39.27	29.36
<b>Spectrum 4</b>		48.20	15.33	36.47

a)



	Element concentration in wt.%				
	C	Fe	O	Si	W
<b>Spectrum 1</b>	3.77	1.02	32.56	2.86	59.79
<b>Spectrum 2</b>	4.49	0.86	9.12		85.53
<b>Spectrum 3</b>	8.13	39.19	10.41		42.26
<b>Spectrum 4</b>		58.35	7.00		34.65
<b>Spectrum 5</b>		62.93	9.36		27.70

b)

**Fig. 12.** SEM images and EDX spot analyses showing the worn surface and its element concentration after DSRW test: a) sample 1,6, and b) sample 1,6 UF.

Due to the presence of those pits, it is assumed that W-rich hard phases have been torn out. SEM images across the worn contact area indicate a partially fractured surface for those cavities (see

Fig. 12a: spots next to spectrum1 and 2, or Fig. 12b: spots next to spectrum 1, 2 and 3). EDX analysis evaluates an increased content of tungsten across the fractured surface area, inter alia, some honeycomb structures are visible. Grooves or scratch marks have only been discovered occasionally. Furthermore, it is found that asperities across the worn surfaces for both sample types were smoothed.

A distinction must be made between those tribological tests where the abrasive is loose as it passes over the surface and those where the abrasive is fixed in orientation as it passes over the surface [47]. In terms of the DSRW test, the abrasive traverses through the contact area either by rolling or by becoming embedded into the rubber wheel and being dragged through surface material and form a groove. However, the abrasive particles pass through the contact area between the wheel and the sample surface only once. Nevertheless, the operating mechanism, and consequently the resulting stress state at the surface mainly depends on the particle motion. Accordingly, different operation mechanisms appear in Taber Abraser and DSRW tests. Abrasion due to grooving takes place where the orientation of the particles is fixed (more likely for the Taber Abraser test). It is reported by Hutchings [48] that these conditions typically generate wear rates a factor of ten greater than comparable tests with loose abrasives. In the event that abrasive particles are embedded, the attack angle of particles is high, which in turn promotes microcutting as main mechanism for the material removal [49, 50]. Regarding a low attack angle, the abrasive particles tend to deform the surface by ploughing with much lower rates of material removal [50]. It is reported that during DSRW test, particle rolling is more pronounced by applied low loads. In contrast, at high loads grooving due to particle sliding is favored. However, it is assumed that the coarse grain-sized silica particles, which serve as abrasive for the DSRW test, are able to orient themselves which again results in a reduced attack angle, and promote ploughing (or microploughing) as predominant operating mechanism.

Regarding size effects such as the carbide particle size across the deposits in relation to the size of the abrasives embedded in the

abrading wheel (Taber Abraser test:  $d_{p50} = 16.24 \mu\text{m}$ ) and using for the DSRW test ( $d_{p50} = 252.70 \mu\text{m}$ ), the operating mechanism (particle impact) is getting more complex. Gong et al. [51] examined the relationship among WC particle size, the deposit microstructure, and the three-body abrasive wear rates by rounded quartz grains using the DSRW test. After testing, pits have been observed and many fine carbide particles were lost in the coating containing a reduced carbide grain size, which resulted in the highest wear rate for the fine carbide grain size reinforced coating. The authors mentioned that the operating mechanisms of the abrasive particles are attributed to micro-cutting and delamination. As the abrasives rolled on the sample surface, dislocation accumulate to a certain depth below the surface, and micro-cracks may have been initiated at defects in the region of the maximum cyclic shear stress. The propagation of micro-cracks had led to material loss. The authors also emphasize the relevance of decarburization and dissolution processes and its effect on the plasticity of the coating, in particular of the metallic binder. Since the sample 1,6 UF is more prone to form eta carbides and to obtain a larger amount of W and C dissolved into the Fe-rich matrix, it can be stated that plasticity of the metallic binder phase of sample 1,6 UF is more reduced.

In another study, Vencl et al. [52] investigated the wear behavior of four different types of hardfaced and thermal sprayed coatings, which featured different carbides. The findings observed in abrasive wear test encouraged the assumption that the wear performance is attributed, inter alia, to the different type and morphological characteristics of the reinforcing particles. Accordingly, the authors showed that the interaction between the size of reinforcing WC particles, average size of abrasive particles, and consequently the abrasive groove depth significantly affect the abrasive wear. In fact, the lowest wear rate was found for a WC reinforced NiFeBSi coating, which exhibited the lowest macrohardness. However, the size of the reinforcing WC particles was greater than the average size of the abrasive particles, which influence the formation of grooves, when the abrasive particles were dragged through surface of the test specimens.

## 5. CONCLUSION

Within the scope of this research, the influence of the carbide grain size fraction on the tribological behavior of arc-sprayed iron-based WC-W<sub>2</sub>C reinforced coatings was analyzed. The dry sliding experiments and the two abrasion tests selected appear to stress the surface of the coatings in a different manner.

With respect to the dry sliding behavior, it is found that the increased amount of a fine proportion of W-rich hard phases, which was provided by the use of a fine carbide grain size fraction as filling, leads to an enhanced wear resistance against sliding. The reason stated is that the cycle loads within the ball-on-disk test are spread to a larger amount of fine distributed W-rich hard phases. Furthermore, samples produced with a fine carbide grain size fraction exhibit a reduced friction, which was revealed by a lower COF.

In terms of the Taber Abraser test, it is demonstrated that a fine carbide grain size fraction used for coating deposition, causes an improved wear resistant against abrasion. As opposed to that, the DSRW test reveals a poorer resistance against abrasive wear. The findings show that the operating mechanisms (abrasive particle impact) affect the stressed surface in a different way, leading either to microcutting or microploughing. Accordingly, the observation of wear marks indicates that the stressed surfaces experience material removal due to cutting or breakouts of fragmented W-rich hard phase.

## Acknowledgement

The authors gratefully acknowledge the financial support of the DFG (German Research Foundation) within the Collaborative Research Centre SFB 708 subproject A1. The contributions of DURUM Verschleisschutz GmbH are gratefully acknowledged for their support in providing the feedstock. The authors would like to thank the DELTA machine group for providing synchrotron radiation.

## REFERENCES

- [1] Q. Yang, T. Senda and A. Ohmori, 'Effect of carbide grain size on microstructure and sliding

- wear behavior of HVOF-sprayed WC-12% Co coatings', *Wear*, vol. 254, pp. 23-34, 2003.
- [2] Q. Wang, Z.H. Chen, and Z.X. Ding, 'Performance of abrasive wear of WC-12Co coatings sprayed by HVOF', *Tribol. Int.*, vol. 42, no. 7, pp. 1046-1051, 2009.
- [3] A. Karimi, C. Verdon, J.L. Martin and R.K. Schmid, 'Slurry erosion behaviour of thermally sprayed WC-M coatings', *Wear*, vol. 186-187, Part 2, pp. 480-486, 1995.
- [4] G.C. Saha, T.I. Khan and G.A. Zhang, 'Erosion-corrosion resistance of microcrystalline and near-nanocrystalline WC-17Co high velocity oxy-fuel thermal spray coatings', *Corros. Sci.*, vol. 53, no. 6, pp. 2106-2114, 2011.
- [5] N. Ma, L. Guo, Z. Cheng, H. Wu, F. Ye and K. Zhang, 'Improvement on mechanical properties and wear resistance of HVOF sprayed WC-12Co coatings by optimizing feedstock structure', *Appl. Surf. Sci.*, vol. 320, pp. 364-371, 2014.
- [6] P.H. Shipway, D.G. McCartney and T. Sudprasert, 'Sliding wear behaviour of conventional and nanostructured HVOF sprayed WC-Co coatings', *Wear*, vol. 259, no. 7-12, pp. 820-827, 2005.
- [7] E. Sánchez et al., 'Microstructure and wear behavior of conventional and nanostructured plasma-sprayed WC-Co coatings', *J. Therm. Spray Technol.*, vol. 19, no. 5, pp. 964-974, 2010.
- [8] X.Q. Zhao, H.D. Zhou and J.M. Chen, 'Comparative study of the friction and wear behavior of plasma sprayed conventional and nanostructured WC-12%Co coatings on stainless steel', *Mater. Sci. Eng.*, A 431, no. 1-2, pp. 290-297, 2006.
- [9] J. Berghaus, B. Marple and C. Moreau, 'Suspension Plasma Spraying of Nanostructured WC-12Co Coatings', *J. Therm. Spray Technol.*, vol. 15, no. 4, pp. 676-681, 2006.
- [10] A.P. Newbery, P.S. Grant, and R.A. Neiser, 'The Velocity and Temperature of Steel Droplets During Electric Arc Spraying', *Surf. Coat. Technol.*, vol. 195, pp. 91-101, 2005.
- [11] I. Gedzevicius and A.V. Valiulis, 'Analysis of Wire Arc Spraying Process Variables on Coatings Properties', *J. Mater. Process. Technol.*, vol. 175, pp. 206-211, 2006.
- [12] P. Sheppard and H. Koiprasert, 'Effect of W Dissolution in NiCrBSi-WC and NiBSi-WC Arc Sprayed Coatings on Wear Behaviors', *Wear*, vol. 317, pp. 194-200, 2014.
- [13] D.J. He, B.J. Fu, J.M. Jiang and X.J. Li, 'Microstructure and Wear Performance of Arc Sprayed Fe-FeB-WC Coatings', *J. Therm. Spray Technol.*, vol. 17, pp. 757-761, 2008.
- [14] W. Tillmann, B. Klusemann, J. Nebel and B. Svendsen, 'Analysis of the Mechanical Properties of an Arc-Sprayed WC-FeCSiMn Coating: Nanoindentation and Simulation', *J. Therm. Spray Technol.*, vol. 20, pp. 328-335, 2011.
- [15] W. Tillmann, W. Luo and U. Selvadurai, 'Wear Analysis of Thermal Spray Coatings on 3D Surfaces', *J. Therm. Spray Technol.*, vol. 23, no. 1-2, pp. 245-251, 2014.
- [16] B. Xu, Z. Zhu, S. Ma, W. Zhang and W. Liu, 'Sliding wear behavior of Fe-Al and Fe-Al/WC coatings prepared by high velocity arc spraying', *Wear*, vol. 257, pp. 1089-1095, 2004.
- [17] P. Niranatumpom and H. Koiprasert, 'Phase transformation of NiCrBSi-WC and NiBSi-WC arc sprayed coatings', *Surf. Coat. Technol.*, vol. 206, no. 2-3, pp. 440-445, 2011.
- [18] D.G. Atteridge, R. Davis, M. Scholl, G. Tewksbury, M. Becker, R. Travis and J.H. Puget, 'Twin wire arc and high energy plasma spray coating using nanometer scale WC-Co in powder-filled cored wire', *J. Therm. Spray Technol.*, vol. 10, no. 1, pp. 176-177, 2001.
- [19] G. Bolelli, T. Börner, F. Bozza, V. Cannillo, G. Cirillo and L. Lusvarghi, 'Cermets coatings with Fe-based matrix as alternative to WC-CoCr: Mechanical and tribological behaviours', *Surf. Coat. Technol.*, vol. 206, no. 19-20, pp. 4079-4094, 2012.
- [20] "Commission Regulation (EC) No 790/2009: amending, for the purposes of its adaptation to technical and scientific progress, Regulation (EC) No 1272/2008 of the European Parliament and of the Council on classification, labelling and packaging of substances and mixtures", Official Journal of the European Union 5.9.2009, L235/1. Available online at: <http://eur-lex.europa.eu/LexUriServ/LexUriServ.do?uri=OJ:L:2009:235:0001:0439:EN:PDF>, accessed 21.03.2017.
- [21] U.S. Department of Health and Human Services, Cobalt-Tungsten Carbide: Powders and Hard Metals, 14th Report on Carcinogens, Available online at: <http://ntp.niehs.nih.gov/?objectid=03C9AF75-E1BF-FF40-DBA9EC0928DF8B15>, accessed 21.03.2017.
- [22] S. Kaielerle, 'Review on Laser Deposition Welding: From Micro to Macro', *Phys. Procedia*, vol. 39, pp. 336-345, 2012.
- [23] S.W. Huang, 'Abrasive Wear Performance and Microstructure of Laser Clad WC/Ni Layers', *Wear*, vol. 256, pp. 1095-1105, 2004.

- [24] M. Jones, 'The Influence of Carbide Dissolution on the Erosion-Corrosion Properties of Cast Tungsten Carbide/Ni-Based PTAW Overlays', *Wear*, vol. 271, pp. 1314-1324, 2011.
- [25] C. Krywka, C. Sternemann, M. Paulus, N. Javid, R. Winter, A. Al-Sawalmih, S. Yi, D. Raabe and M. Tolan, 'The small-angle and wide-angle x-ray scattering setup at beamline BL9 of DELTA', *J. Synchrotron Radiat.*, vol. 14, pp. 244-251, 2007.
- [26] A. Hammersley, S. Svensson, M. Hanfland, A. Fitch and D. Hausermann, 'Two-dimensional detector software: from real detector to idealised image or two-theta scan', *Int. J. High Pressure Res.*, vol. 14, pp. 6235-6248, 1996.
- [27] ASTM standards G65-04 *Standard test method for measuring abrasion using the dry sand/rubber wheel apparatus*, 2004
- [28] W.C. Oliver and G.M. Pharr, 'An improved technique for determining hardness and elastic modulus using load and displacement sensing indentation experiments', *J. Mater. Res.*, vol. 7, pp. 1564-1583, 1992.
- [29] J. Musil, F. Kunc, H. Zeman and H. Poláková, 'Relationships between hardness, Young's modulus and elastic recovery in hard nanocomposite coatings', *Surf. Coat. Technol.*, vol. 154, pp. 304-313, 2002.
- [30] F. Cai, X. Huang and Q. Yang, 'Mechanical properties, sliding wear and solid particle erosion behaviors of plasma enhanced magnetron sputtering CrSiCN coating systems', *Wear*, vol. 324-325, pp. 27-35, 2015.
- [31] V. Lovelock, 'Powder/processing/structure relationships in WC-Co thermal spray coatings: A review of the published literature', *J. Therm. Spray Technol.*, vol. 7, pp. 357-373, 1998.
- [32] D. Suetin, I. Shein and A. Ivanovskii, 'Structural, Electronic and Magnetic Properties of Eta Carbides (Fe<sub>3</sub>W<sub>3</sub>C, Fe<sub>6</sub>W<sub>6</sub>C, Co<sub>3</sub>W<sub>3</sub>C and Co<sub>6</sub>W<sub>6</sub>C) From First Principles Calculations', *Physica B*, vol. 404, pp. 3544-3549, 2009.
- [33] Y. Li et al., 'First-principles study on the stability and mechanical property of eta M<sub>3</sub>W<sub>3</sub>C (M=Fe, Co, Ni) compounds', *Physica B*, vol. 405, pp. 1011-1017, 2010.
- [34] Y. Liu, Y. Jiang, R. Zhou and J. Feng, 'First-principles calculations of the mechanical and electronic properties of Fe-W-C ternary compounds', *Comp. Mater. Sci.*, vol. 82, pp. 26-32, 2014.
- [35] A. Do Nascimento, V. Ocelik, M. Ierardi and J. De Hosson, 'Wear resistance of WC p/Duplex Stainless Steel metal matrix composite layers prepared by laser melt injection', *Surf. Coat. Technol.*, vol. 202, pp. 4758-4765, 2008.
- [36] A. Do Nascimento, V. Ocelik, M. Ierardi, J. De Hosson, 'Microstructure of reaction zone in WC p/duplex stainless steels matrix composites processing by laser melt injection', *Surf. Coat. Technol.*, vol. 202, pp. 2113-2120, 2008.
- [37] S. Zhou and X. Dai, 'Microstructure evolution of Fe-based WC composite coating prepared by laser induction hybrid rapid cladding', *Appl. Surf. Sci.*, vol. 256, pp. 7395-7399, 2010.
- [38] H. Berns, *Stahl und Gusseisen*, Berlin Heidelberg: Springer Verlag, 2013 (in German).
- [39] T. Dash and B. Nayak, 'Preparation of WC-W<sub>2</sub>C composites by arc plasma melting and their characterisations', *Ceram. Int.*, vol. 39, pp. 3279-3292, 2013.
- [40] T. Gerthsen, *Chemie für den Maschinenbau*, Karlsruhe: Universitätsverlag Karlsruhe, 2006 (in German).
- [41] Q.Q. Ren, J.L. Fan, Y. Han and H.R. Gong, 'Structural, thermodynamic, mechanical, and magnetic properties of FeW system', *J. Appl. Phys.*, vol. 116, pp. 093909-1 - 093909-9, 2014.
- [42] Y. Liu, Y. Jiang and J. Feng, 'Mechanical properties and chemical bonding characteristics of WC and W<sub>2</sub>C compounds', *Ceram. Int.*, vol. 40, pp. 2891-2899, 2014.
- [43] H. Taimatsu, S. Sugiyama and Y. Kodaira, 'Synthesis of W<sub>2</sub>C by reactive hot pressing and its mechanical properties', *Mater. Trans.*, vol. 49, pp. 1256-1261, 2008.
- [44] M. Yandouzi, L. Ajdelsztajn and B. Jodoin, 'WC-based composite coatings prepared by the pulsed gas dynamic spraying process: Effect of the feedstock powders', *Surf. Coat. Technol.*, vol. 202, pp. 3866-3877, 2008.
- [45] K. van Acker, D. Vanhoyweghen, R. Persoons and J. Vangrunderbeek, 'Influence of tungsten carbide particle size and distribution on the wear resistance of laser clad WC/Ni coatings', *Wear*, vol. 258, pp. 194-202, 2005.
- [46] W. Tillmann, I. Baumann, P.S. Hollingsworth and L. Hagen, 'Sliding and Rolling Wear Behavior of HVOF-Sprayed Coatings Derived from Conventional, Fine and Nanostructured WC-12Co Powders', *J. Therm. Spray Technol.*, vol. 23, pp. 262-280, 2014.
- [47] S.M. Nahvi, P.H. Shipway and D.G. McCartney, 'Particle motion and modes of wear in the dry sand-rubber wheel abrasion test', *Wear*, vol. 267, no. 11, pp. 2083-2091, 2009.

- [48] I.M. Hutchings, *Tribology—Friction and Wear of Engineering Materials*, London: Edward Arnold, 1992.
- [49] T.O. Mulhearn and L.E. Samuels, 'The abrasion of metals: a model of the process', *Wear*, vol. 5, pp. 478-498, 1962.
- [50] J.M. Challen and P.L.B. Oxley, 'An explanation of the different regimes of friction and wear using asperity deformation models', *Wear*, vol. 53, pp. 229-243, 1979.
- [51] T. Gong, P. Yao, X. Zuo, Z. Zhang, Y. Xiao, L. Zhao, H. Zhou, M. Deng, Q. Wang, A. Zhong, 'Influence of WC carbide particle size on the microstructure and abrasive wear behavior of WC-10Co-4Cr coatings for aircraft landing gear', *Wear*, vol. 362-363, pp. 135-145, 2016.
- [52] A. Vencl, B. Katavić, D. Marković, M. Ristić and B. Gligorijević, 'The Tribological Performance of Hardfaced/Thermal Sprayed Coatings for Increasing the Wear Resistance of Ventilation Mill Working Parts', *Tribology in Industry*, vol. 37, pp. 320-329, 2015.